SUPPLEMENTARY INFORMATION

Iridium single-atom catalyst coupled with lattice oxygen activated $CoNiO_2$ for accelerating oxygen evolution reaction

Meng-Qi Yang[a], Kai-Ling Zhou[*a], Chao Wang[a], Man-Chen Zhang[b], Chang-Hao Wang[a], Xiaoxing Ke[b], Ge Chen[c], Hao Wang[a] and Ru-Zhi Wang[*a]

a) Institute of Advanced Energy Materials and Devices, Faculty of Materials and Manufacturing; Key Laboratory of Advanced Functional Materials of Education Ministry of China, Beijing University of Technology, Beijing 100124, China.

b) Institute of Microstructure and Property of Advanced Materials, Faculty of Materials and Manufacturing, Beijing University of Technology, Beijing 100124, China

c) Beijing Key Laboratory for Green Catalysis and Separation, College of Environmental & Energy Engineering, Beijing University of Technology, Beijing 100124, China

[*]email: wrz@bjut.edu.cn; zkling@bjut.edu.cn.

Experimental details

Synthesis of V_O-$CoNiO_2$ nanosheets. Prior to preparation, the stainless steel substrate (SUS304) was firstly polished with sandpaper to form a coarse surface and subsequently was sonicated in HCl solution (5 M) for 10 min. Next, the clean substrate was repeatedly washed with deionized water and alcohol. The deposition was carried out by a typical three-electrode system with the stainless steel substrate as the working electrode, a graphite sheet utilized as a counter electrode and a saturated calomel serving as a reference electrode (SCE) in a precursor solution consisting of 70 mM $NiCl_2 \cdot 6H_2O$, 70 mM $CoCl_2 \cdot 6H_2O$, 1 mM $AlCl_3 \cdot 9H_2O$ and 92 mM H_3BO_3 at the room temperature. To optimize the chemical compositions of Al doped CoNi alloy. The electrodeposition process was carried out through constant potential electrolysis at -1.2 V for 200 s using 660E potentiostat (Shanghai Chenhua Apparatus Co., Ltd., China). The Al doped CoNi alloy electrode with a loading mass of 0.23 mg cm^{-2} was heated at 400 ^oC with a heating rate about 5 ^oC min^{-1} and then maintained for 30 mins in a tube furnace under air atmosphere. Then, Al doped V_O-$CoNiO_2$ supported on stainless steel substrate was immersed in 5 M NaOH solution under continuous stirring for 24 h to etch Al ions. As-prepared V_O-$CoNiO_2$ electrodes were rinsed with deionized water, and then dried at room temperature.

Synthesis of Ir_{SA}-V_O-$CoNiO_2$ nanosheets. The Ir single atom deposition on V_O-$CoNiO_2$ nanosheets was carried out by a typical three-electrode system and a Hg/HgO electrode was utilized as the reference electrode. The precursor solution consisted of 100 μM $IrCl_4$ and 1 M KOH at the room temperature. The electrochemical depositions were carried out from 0.10 V to -0.40 V versus RHE for twenty periods with a sweeping rate of 5mV s^{-1}. Finally, the electrode was washed by deionized water and dried at room temperature.

Synthesis of $CoNiO_2$ nanosheets. $CoNiO_2$ is prepared by the same method compared to V_O-$CoNiO_2$ except for the annealing process at 500 ^oC for 30 min.

Synthesis of Ir_{SA}-$CoNiO_2$ nanosheets. Ir_{SA}-$CoNiO_2$ is prepared by the same method compared to Ir_{SA}-V_O-$CoNiO_2$ except for the annealing process at 500 ^oC for 30 min.

Synthesis of $Ir_{cluster}$-$CoNiO_2$ nanosheets. Ir_{SA}-$CoNiO_2$ is prepared by the same method compared to Ir_{SA}-V_O-$CoNiO_2$ except for the electrochemical depositions of Ir for thirty periods.

Characterizations. The crystal phase of electrodes was explored using the Shimadzu X-ray diffractometer (XRD, Bruker, D8 Advance Davinci) with Cu Kα source and Raman Spectrophotometer (LabRAM HR Evolution) with an exciting wavelength of 532nm. The chemical valence of elements was analyzed by XPS measurement (ESCA-LAB 250Xi). The nanostructural morphology of electrodes was observed by field-emission scanning electron microscopy (FE-SEM SU-70, Japan). HRTEM images, HAADF-STEM images, and STEM-EDS mapping images were obtained by an FEI Titan G^2 microscope equipped with an aberration corrector for probe-forming lens and a Bruker SuperX energy dispersive spectrometer operated at 300 kV. The EXAFS measurement of the Ir_{SA}-V_O-$CoNiO_2$ and Ir_{SA}-$CoNiO_2$ at the Ir L_3-edge was performed at 1W1B station at the Beijing Synchrotron Radiation Facility. Data analysis and fitting were performed with Athena and Artemis in the Demeter package.

Electrochemical measurements. The electrochemical measurements were conducted by a standard three-electrode cell with the connection of an electrochemical workstation. As-synthesized Ir_{SA}-Vo-$CoNiO_2$ nanosheets was employed as the working electrode. A graphite rod was applied as the counter electrode. Hg/HgO electrode was utilized as the reference electrode. The potentials were converted to RHE by the equation, $E_{RHE} = E_{Hg/HgO} + 0.059\ pH + 0.098\ V$. The geometric surface area of the catalysts supported stainless steel is 1 cm^2, corresponding the mass loading of Ir-$CoNiO_2$ nanosheets (2 mg cm^{-2}). The OER polarization curves were measured by a LSV approach with a sweeping rate of 1mV s^{-1} in oxygen-saturated 1M KOH media at 25 °C. EIS was performed within the frequency range from 100 kHz to 0.1 Hz. The electrochemical double-layer capacitance (C_{dl}) was measured at the non-Faradaic potential from 0.9 to 1 V s. RHE at the various scan rates of 20, 40, 60, 80, 100 to estimate the actual electrochemical surface area (ECSA).

The TOF values can be obtained by utilizing the following equation.

$$\mathrm{TOF}=\frac{\#\text{Total Oxygen Turn Overs per geometric area}}{\#\text{Active Sites per geometric area}}$$

$$\mathrm{O_2}=\left(\mathrm{j}\frac{\mathrm{mA}}{\mathrm{cm^2}}\right)\left(1\frac{\mathrm{C/s}}{1000\ \mathrm{mA}}\right)\left(\frac{1\ \mathrm{mol\ e^-}}{96485.3\ \mathrm{C}}\right)\left(\frac{1\ \mathrm{mol\ O_2}}{4\ \mathrm{mol\ e^-}}\right)\left(\frac{6.02\times10^{23}\ \mathrm{molecules\ O_2}}{1\ \mathrm{mol\ O_2}}\right)$$

$$=1.56\times10^{15}|j|\mathrm{O_2(s\times cm^2)^{-1}}$$

$$\text{Active Sites}=\left(\frac{\text{mass loading}\times\text{catalyst loading per geometric area}\left(\mathrm{g/cm^2}\right)}{\text{Ir Mw}\left(\mathrm{g/mol}\right)}\right)\left(\frac{6.02\times10^{23}\ \text{Ir atoms}}{1\text{mol Ir}}\right)$$

$$=\left(\frac{0.86\ \text{wt\%}\times 0.02\ \text{g/cm}^2}{192.2\ \text{g/mol}}\right)\left(\frac{6.02\times 10^{23}\ \text{Ir atoms}}{1\text{mol Ir}}\right)=5.39\times 10^{16}\ \ {}^{\text{sites}}/_{\text{cm}^2}$$

Density functional theory calculation. VASP code was used in our Density functional theory (DFT) calculation. The electron exchange-correlation potential was conducted by the Perdew-Burke-Ernzerhof (PBE) functional of generalized gradient approximation (GGA). The kinetic energy cutoff was set to 500 eV for the plane-wave basis set. Brillouin zone integration was sampled with the 4 × 4 × 4 and 4 ×4 × 1 MonkhorstPack mesh k-point for bulk and surface calculations, respectively. The $CoNiO_2$ (111), the strongest crystal plane of XRD Characterization, was constructed by a periodic six-layer slab repeated in 2 × 2 surface unit cell with a vacuum region of 15 Å along with the Z axis. The Co atom was also superseded by Ir atom used to construct the Ir_{SA}-$CoNiO_2$ based on the XRD characterizations. Meanwhile, the oxygen vacancy of $CoNiO_2$ (111) was also construct by remove oxygen atoms during the structural optimization process. The total energy convergence tolerances were set to 1 × 10^{-5} eV and 0.001 eV $Å^{-1}$ for force tolerance. The Gibbs free energy changes for the water oxidation steps using AEM and LOM mechanisms were calculated using the following Equations (S1-S5) and (S6-10), respectively.

$$\Delta G_1=\Delta G_{O^*}-\Delta G_{OH^*}+\Delta E_{ZPE}-T\Delta S \quad (S1)$$

$$\Delta G_2=\Delta G_{OOH^*}-\Delta G_{O^*}+\Delta E_{ZPE}-T\Delta S \quad (S2)$$

$$\Delta G_3=\Delta G_{OO^*}-\Delta G_{OOH^*}+\Delta E_{ZPE}-T\Delta S \quad (S3)$$

$$\Delta G_4=4.92\text{eV}-\Delta G_{OO^*}+\Delta E_{ZPE}-T\Delta S \quad (S4)$$

$$\Delta G_5=\Delta G_{OH^*}+\Delta E_{ZPE}-T\Delta S \quad (S5)$$

$$\Delta G_1=\Delta G_{[O\text{-}O+O_v]^*}-\Delta G_{OH^*}+\Delta E_{ZPE}-T\Delta S \quad (S6)$$

$$\Delta G_2=\Delta G_{[O\text{-}O+H^v]^*}-\Delta G_{[OO+V_O]^*}+\Delta E_{ZPE}-T\Delta S \quad (S7)$$

$$\Delta G_3=4.92\text{eV}+\Delta G_{[V_O+H^v]^*}-\Delta G_{[O\text{-}O+H^v]^*}+\Delta E_{ZPE}-T\Delta S \quad (S8)$$

$$\Delta G_4=\Delta G_{[OH^*+H^v]}-\Delta G_{[V_O+H^v]^*}+\Delta E_{ZPE}-T\Delta S \quad (S9)$$

$$\Delta G_5=\Delta G_{OH^*}-\Delta G_{[OH^*+H^v]}+\Delta E_{ZPE}-T\Delta S \quad (S10)$$

Herein, ΔE_{ZPE} is the zero point energy difference between the adsorption state and gas state, T is the temperature (298.15 K), ΔS is the entropy various between the adsorption and gas phase.

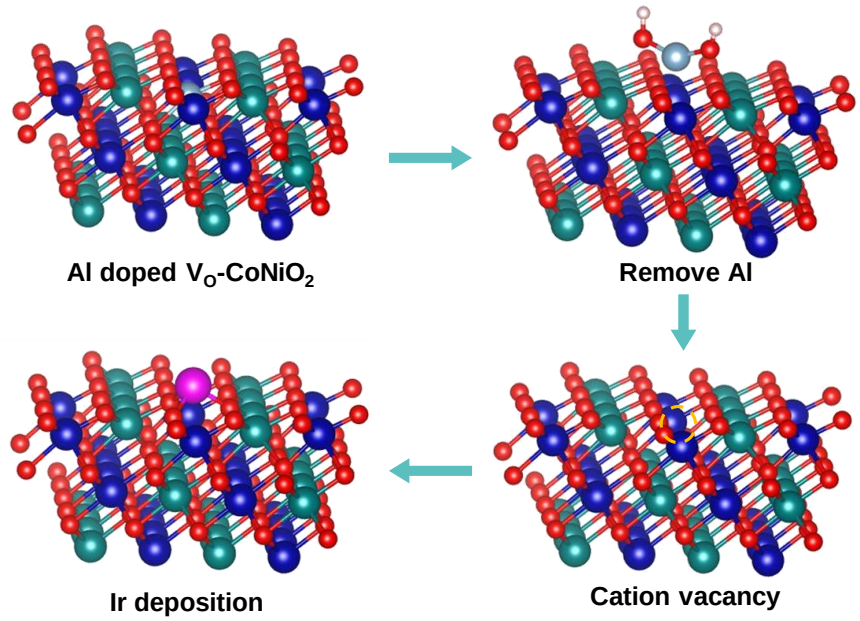

Fig. S1 Schematic illustration of the adding and removing Al process during the catalyst preparation.

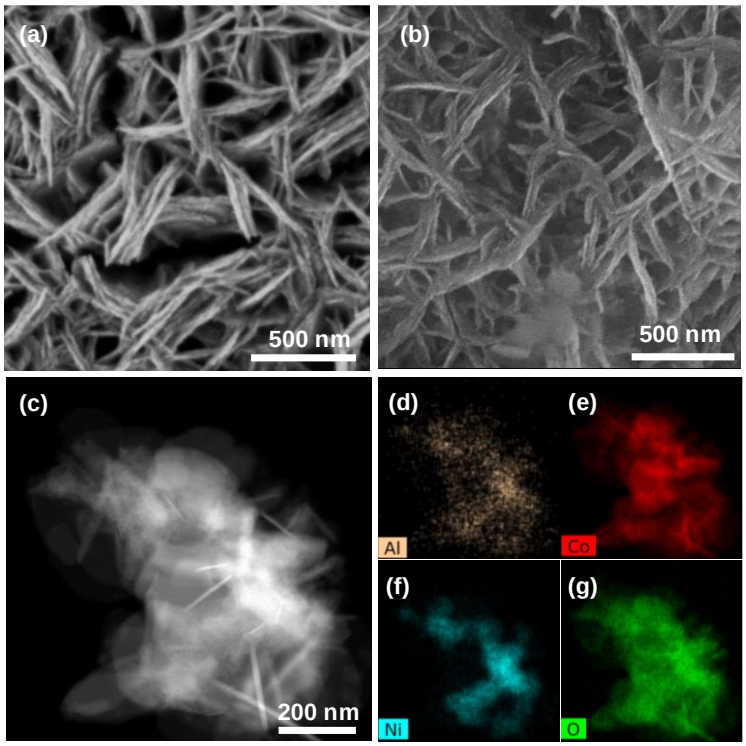

Fig. S2 SEM images of (a) Al-doped V_O-$CoNiO_2$ and (b) V_O-$CoNiO_2$. (c) HAADF-STEM image of Al-doped V_O-$CoNiO_2$. (d-g) Elemental mapping of Al-doped V_O-$CoNiO_2$.

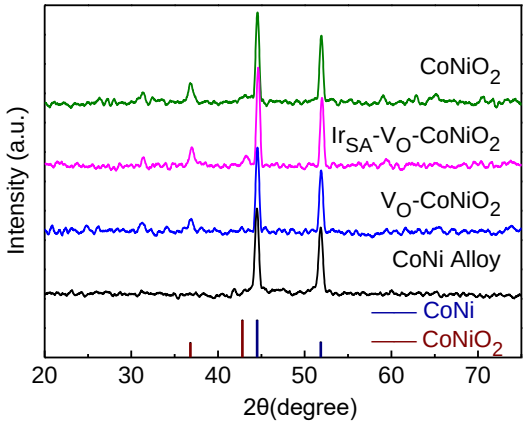

Fig. S3 XRD patterns of CoNi alloy, V_O-$CoNiO_2$, Ir_{SA}-V_O-$CoNiO_2$ and $CoNiO_2$.

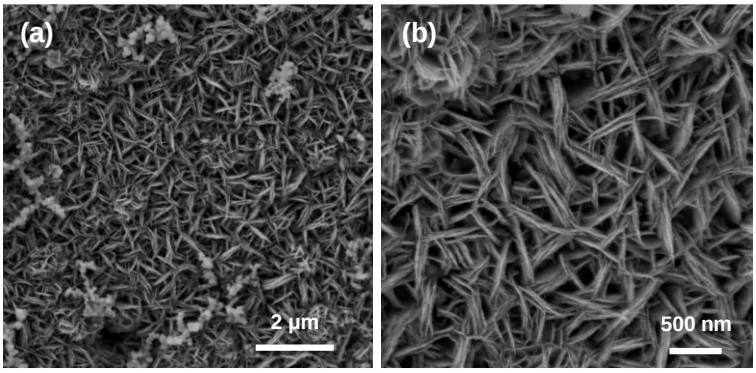

Fig. S4 Additional SEM images of CoNi alloy. (a) Low magnification and (b) high magnification.

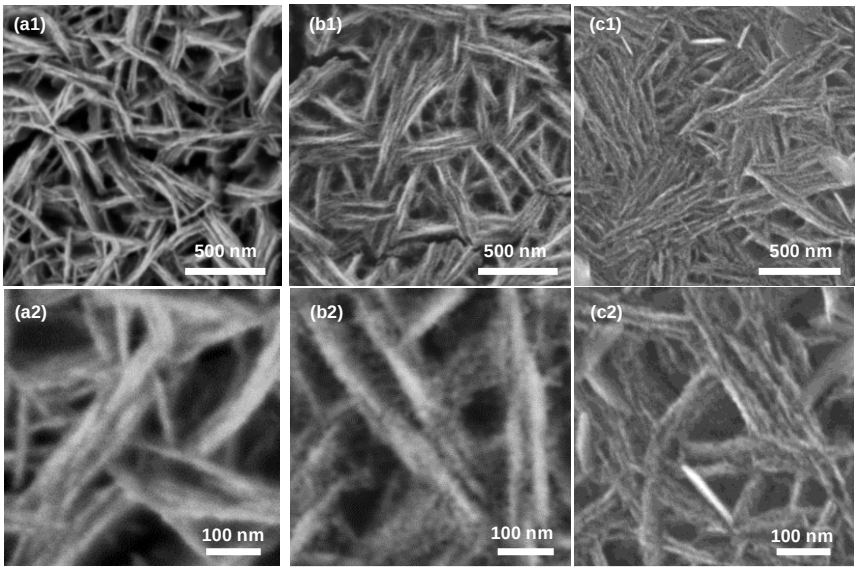

Fig. S5 The SEM image of samples (a1-2) V_O-$CoNiO_2$, (b1-2) $CoNiO_2$, and (c1-2) Ir_{SA}-$CoNiO_2$.

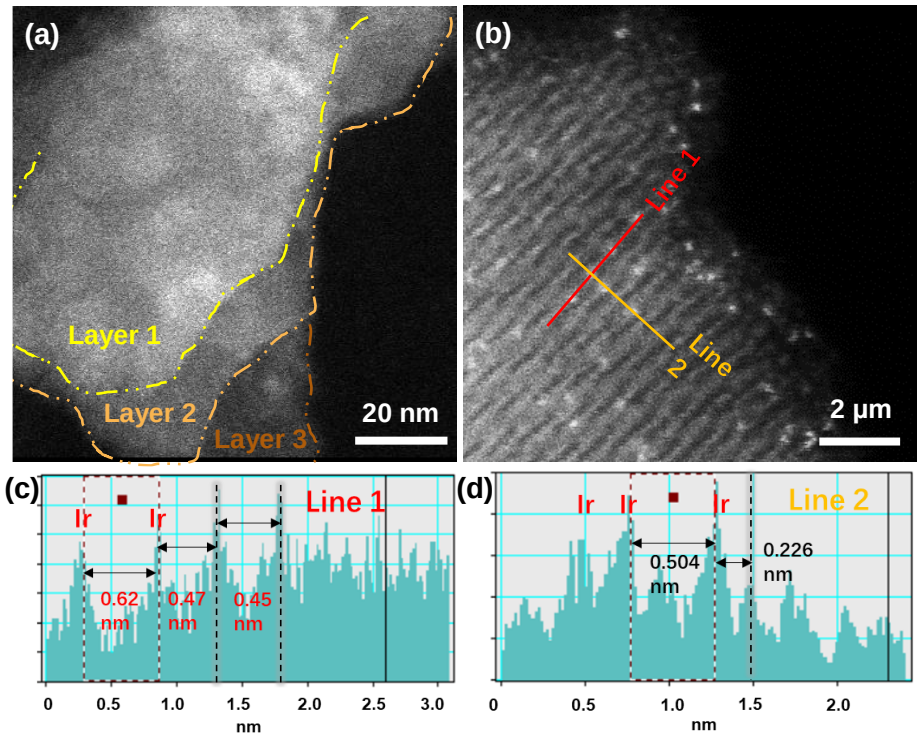

Fig. S6 HAADF-STEM of Ir single atoms. (a) Low-magnification HAADF-STEM image of Ir_{SA}-V_O-$CoNiO_2$. (b) High-magnification HAADF-STEM image of Ir_{SA}-V_O-$CoNiO_2$. (c) The line profiles for HAADF intensity analysis labeled line 1. (d) The line profiles for HAADF intensity analysis labeled line 2.

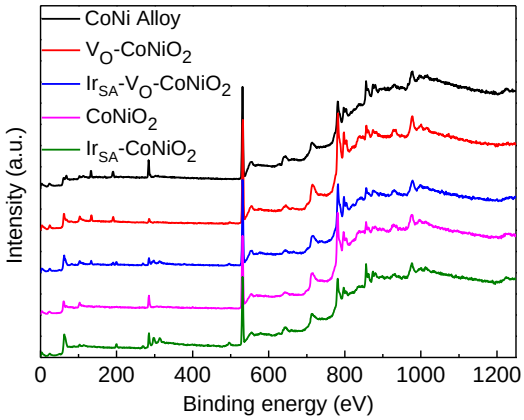

Fig. S7 XPS spectra of CoNi alloy, V_O-$CoNiO_2$, Ir_{SA}-V_O-$CoNiO_2$, $CoNiO_2$, and Ir_{SA}-$CoNiO_2$.

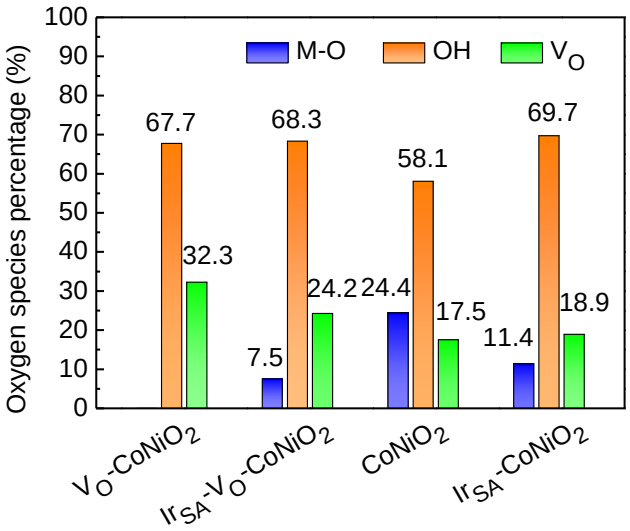

Fig. S8 Quantitative analysis of different oxygen species based on the fitting result of O 1*s* XPS spectra.

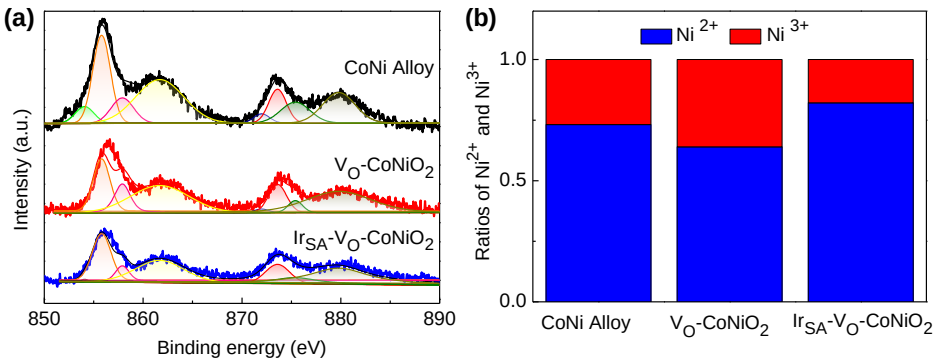

Fig. S9 (a) Ni 2*p* XPS spectra, and (b) ratios of Ni^{2+}/Ni^{3+} of CoNi alloy, V_O-$CoNiO_2$, and Ir_{SA}-V_O-$CoNiO_2$.

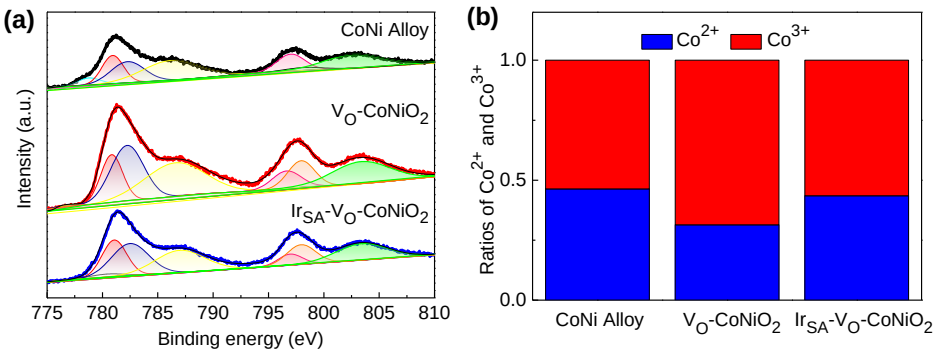

Fig. S10 (a) Co 2*p* XPS spectra, and (b) ratios of Co^{2+}/Co^{3+} of CoNi alloy, V_O-CoNiO$_2$, and Ir_{SA}-V_O-CoNiO$_2$.

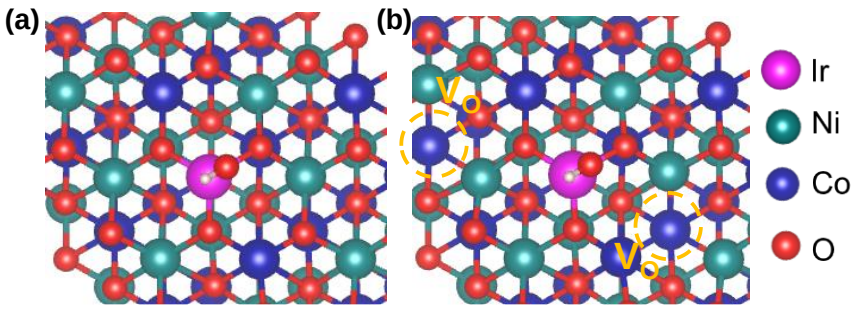

Fig. S11 Model of V_O modulated Ir_{SA}-$CoNiO_2$. (a) Ir_{SA}-$CoNiO_2$, (b) Ir_{SA}-V_O-$CoNiO_2$.

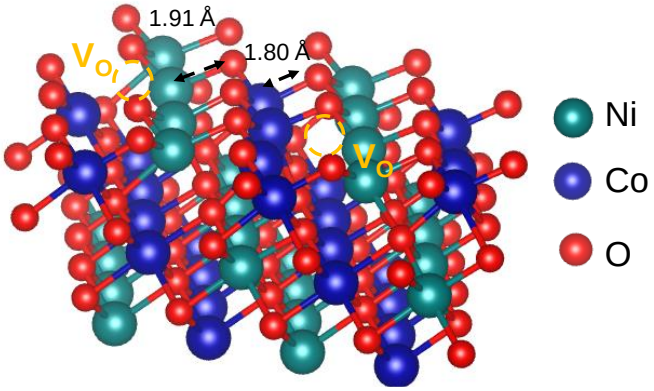

Fig. S12 Structure of V_O-$CoNiO_2$.

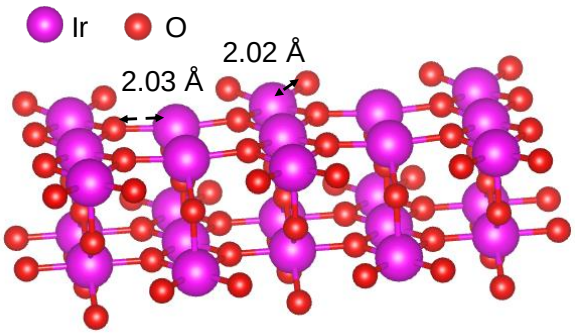

Fig. S13 Structure of IrO_2 (110).

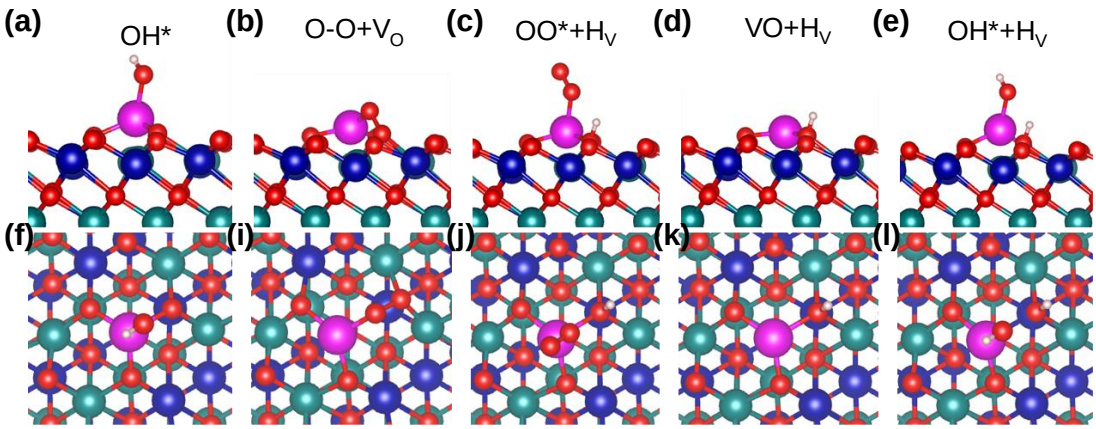

Fig. S14 Configurations for LOM pathway calculations. (a-e) Side views, and (f-l) top views of Ir_{SA}-V_O-$CoNiO_2$.

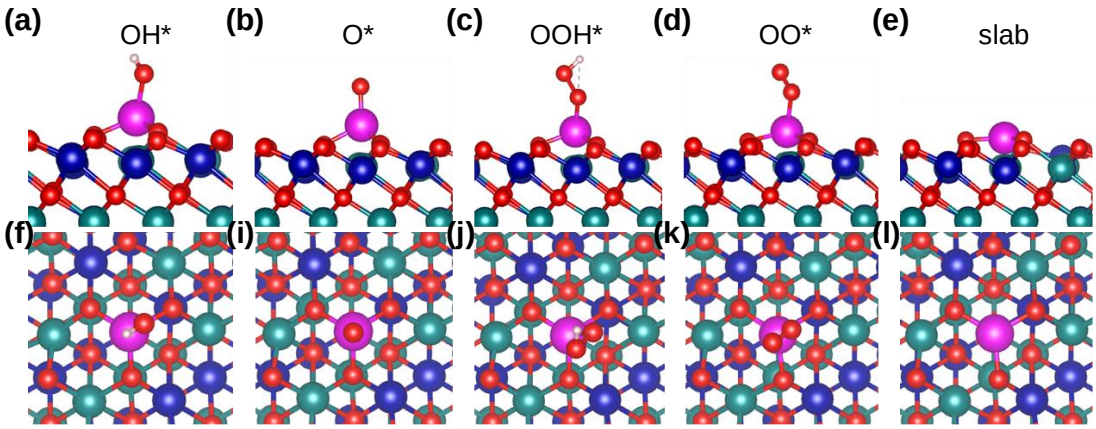

Fig. S15 Configurations for AEM pathway calculations. (a-e) Side views, and (f-l) top views of Ir_{SA}-V_O-$CoNiO_2$.

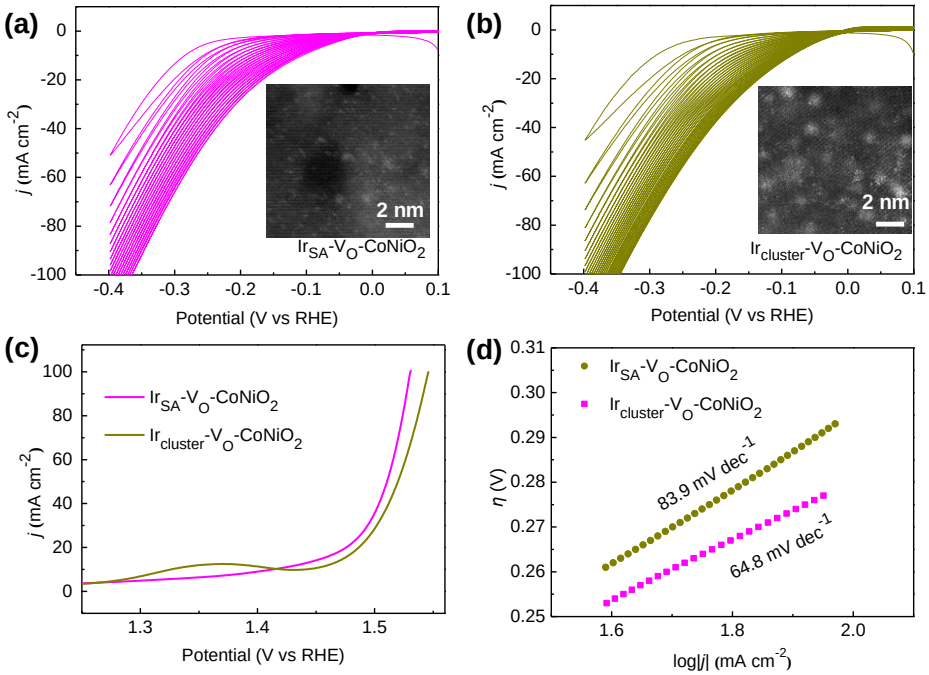

Fig. S16 Ir cluster analysis. Deposition curve of monatomic Ir for (a) Ir_{SA}-V_O-$CoNiO_2$ and (b) $Ir_{cluster}$-V_O-$CoNiO_2$. The inset shows the corresponding HAADF-STEM images of Ir_{SA}-V_O-$CoNiO_2$ in Fig. S16a and $Ir_{cluster}$-V_O-$CoNiO_2$ in Fig. S16b. (c) LSV curves of Ir_{SA}-V_O-$CoNiO_2$ and $Ir_{cluster}$-V_O-$CoNiO_2$. (d) Tafel plots of Ir_{SA}-V_O-$CoNiO_2$ and $Ir_{cluster}$-V_O-$CoNiO_2$.

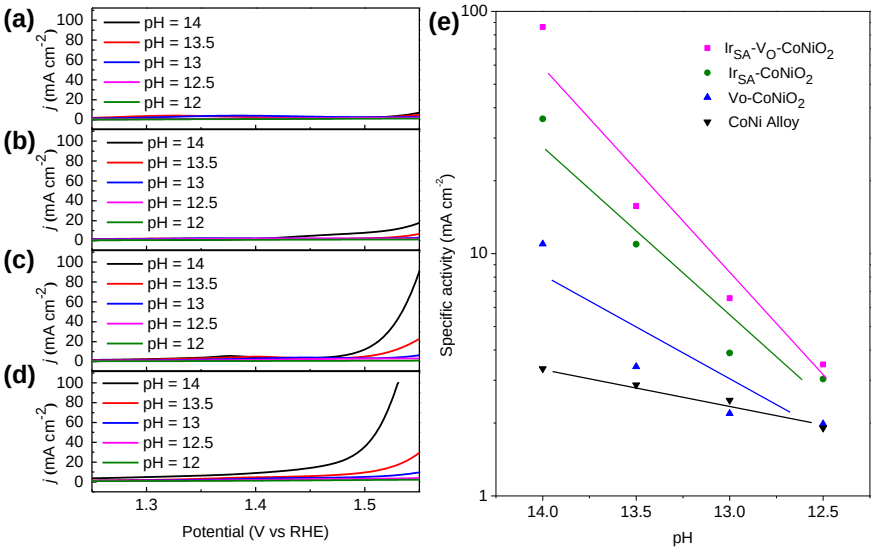

Fig. S17 Experimental verification of Ir_{SA}-V_O-$CoNiO_2$ in via LOM pathway. The pH dependence of the OER activities of (a) CoNi alloy, (b) V_O-$CoNiO_2$, (c) Ir_{SA}-$CoNiO_2$, and (d) Ir_{SA}-V_O-$CoNiO_2$. (e) Current densities of CoNi alloy, V_O-$CoNiO_2$, Ir_{SA}-$CoNiO_2$, and Ir_{SA}-V_O-$CoNiO_2$ at 1.55 V versus RHE as a function of the pH value.

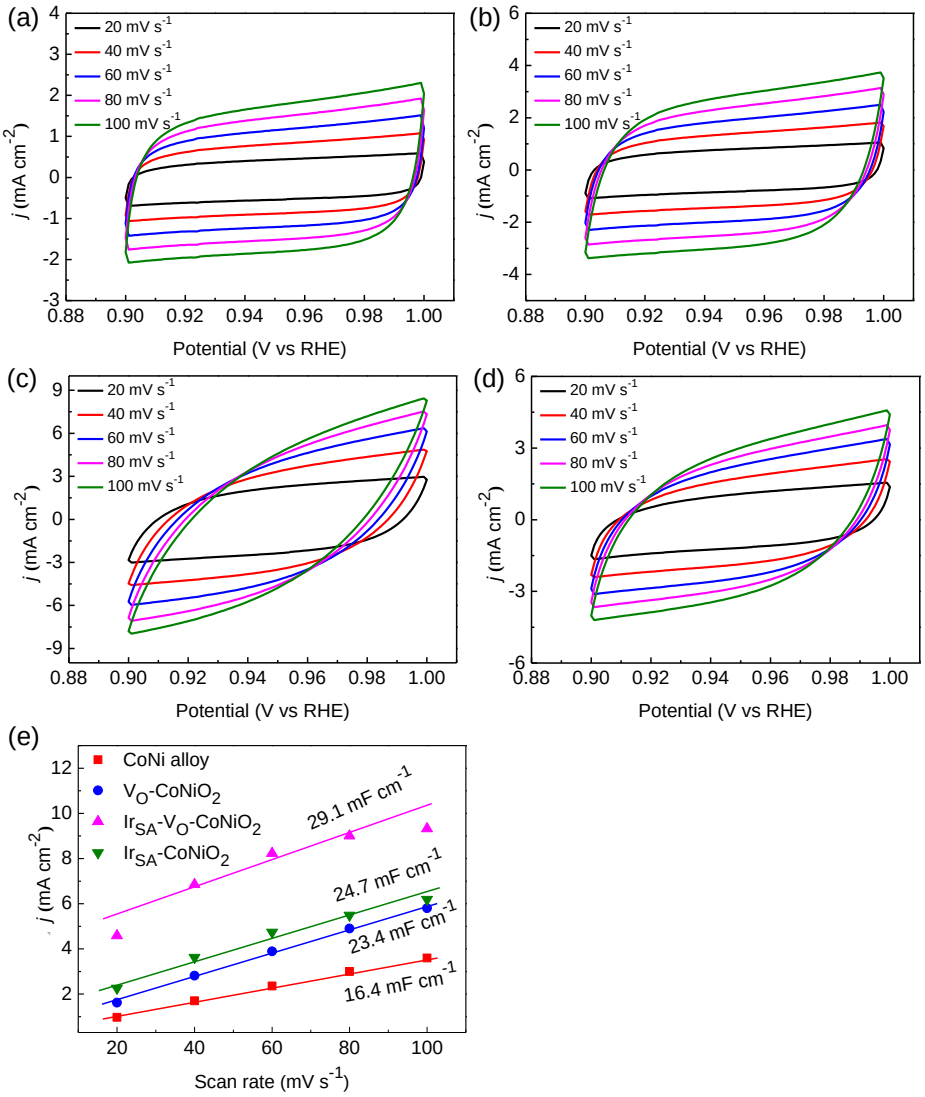

Fig. S18 Cyclic voltammograms (CV) curves and charging current density differences of samples at the scan rates of 20 mV to 100 mV per second. (a) CV of CoNi alloy. (b) CV of V_O-$CoNiO_2$. (c) CV of Ir_{SA}-V_O-$CoNiO_2$. (d) CV of Ir_{SA}-$CoNiO_2$. (e)The corresponding plot for estimating C_{dl} of CoNi alloy, V_O-$CoNiO_2$, Ir_{SA}-V_O-$CoNiO_2$ and Ir_{SA}-$CoNiO_2$.

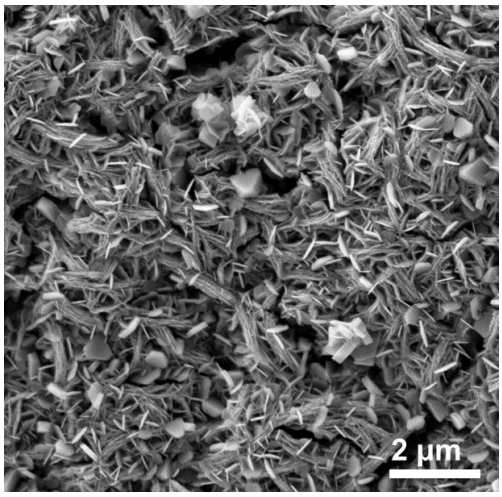

Fig. S19 SEM images of Ir_{SA}-V_O-$CoNiO_2$ after chronoamperometry test for 25 h.

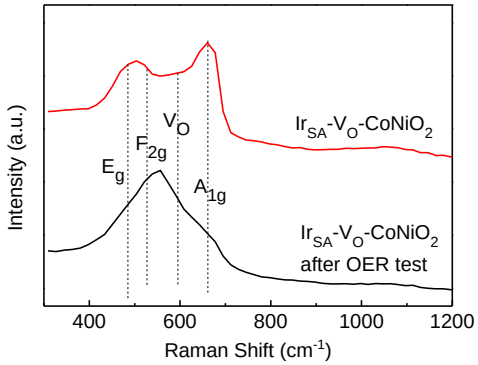

Fig. S20 Raman spectra of Ir_{SA}-V_O-$CoNiO_2$ and Ir_{SA}-V_O-$CoNiO_2$ after OER test.

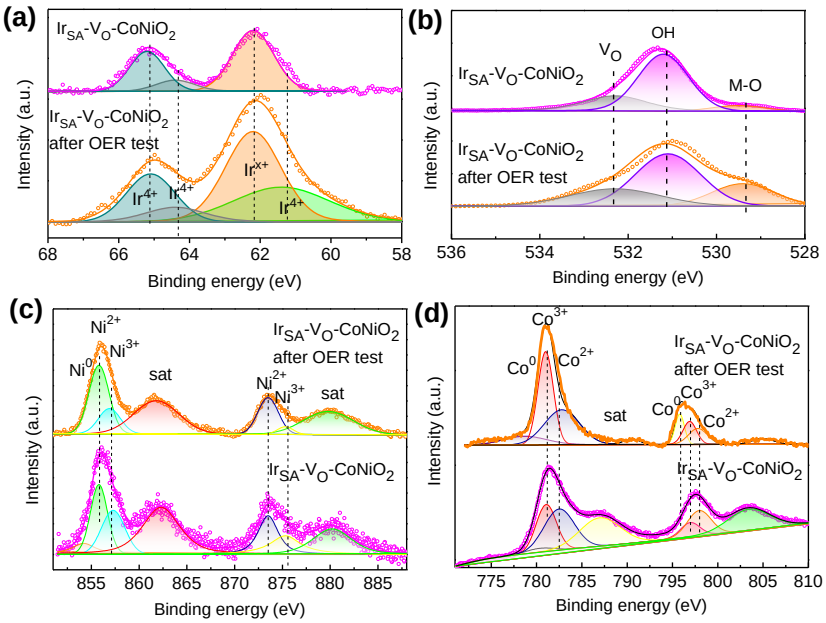

Fig. S21 (a) Ir 4*f*, (b) O 1*s*, (c) Co 2*p*, and (d) Ni 2*p* XPS spectra of Ir_{SA}-V_O-$CoNiO_2$ and Ir_{SA}-V_O-$CoNiO_2$ after OER test.

Table S1 The concentration of Ir, Ni and Co in CoNi alloy, Ir_{SA}-V_O-$CoNiO_2$ and Ir_{SA}-$CoNiO_2$ by ICP-AES measurement.

Sample	Elements	Concentration(mg/L)
CoNi	Co	10.31
	Ni	10.08
	———	———
Ir_{SA}-V_O-$CoNiO_2$	Co	24.26
	Ni	19.04
	Ir	0.475
Ir_{SA}-$CoNiO_2$	Co	17.6
	Ni	15.32
	Ir	0.395

Table S2 Fitting parameters of FT-EXAFS spectra of Ir foil, Ir_{SA}-V_O-$CoNiO_2$, Ir_{SA}-$CoNiO_2$, and IrO_2 catalyst under different conditions (S_0^2=0.60).

Sample	Shell	*CN*	*R*(Å)	σ^2	$\triangle E_0$	R factor
Ir foil	Ir-Ir	12	2.708±0.002	0.0025	8.71±0.64	0.0072
IrO_2	Ir-O	6	1.981±0.008	0.0025	10.85±1.13	0.007
Ir_{SA}-V_O-$CoNiO_2$	Ir-O	4.7±1.3	1.868±0.044	0.009	8.41±2.78	0.025
	Ir-O	7.9±1.4	2.054±0.026	0.006		
Ir_{SA}-$CoNiO_2$	Ir-O	4.4±0.8	2.082±0.013	0.003	17.45±1.38	0.014
	Ir-O	8.7±0.5	2.311±0.026	0.003		

[a]*CN*: coordination numbers; [b]*R*: bond distance; [c]σ^2: Debye-Waller factors; [d] ΔE_0: the inner potential correction. *R* factor: goodness of fit. S_0^2 was set to 0.60, according to the experimental EXAFS fit of Ir foil reference by fixing CN as the known crystallographic value.

Table S3 Bader charge analysis of Ir_{SA}-V_O-$CoNiO_2$ and IrO_2.

sample	Atomic	Bader charge value	Theoretical charge value	Δe
Ir_{SA}-V_O-$CoNiO_2$	Ir	7.351	9	-1.649
	O_{OH}	6.883	6	0.883
	$O_{bottom1}$	6.811	6	0.881
	$O_{bottom2}$	6.836	6	0.836
	$O_{bottom3}$	6.845	6	0.845
IrO_2	Ir	7.586	9	-1.414
	$O_{adjacent1}$	6.855	6	0.855
	$O_{adjacent2}$	6.855	6	0.855
	$O_{adjacent3}$	6.857	6	0.857
	$O_{adjacent4}$	6.857	6	0.857

Table S4 Comparison of the TOF performance with previously reported noble-metal base catalysts.

Catalysts	overpotential (mV)	TOF (O_2 s^{-1})	Ref
Ir_{SA}-V_O-$CoNiO_2$	300	2.87	This work
IrO_2	350	0.04	Ref[1]
RuO_2	350	0.05	Ref[1]
$SrCo_{0.9}Ir_{0.1}O_{3-\delta}$	270	2.56	Ref[2]
$Ir_{18\ wt\ \%}$-NiO	300	1.37	Ref[3]
Ir_1/V_O-CoOOH	300	0.14	Ref[4]
NiIr-LDH	250	0.01	Ref[5]
$Ir_1/CoOOH_{sur}$	300	0.24	Ref[6]
$NiFeIr_{0.03}$/Ni NW@NSs	270	0.05	Ref[7]
Ru-Co/ELCO	330	0.05	Ref[8]
^{s}Au/NiFe LDH	280	0.11	Ref[9]

Table S5 EIS data of CoNi alloy, V_O-$CoNiO_2$, Ir_{SA}-V_O-$CoNiO_2$ and Ir_{SA}-$CoNiO_2$ in OER tests.

Catalysts	R_s (Ω)	R_{ct} (Ω)	CEP-T	CEP-P	R_2 (Ω)	C
CoNi	1.52	0.65	0.26	0.83	0.41	0.55
V_O-$CoNiO_2$	1.67	0.54	0.29	0.93	0.03	0.63
Ir_{SA}-V_O-$CoNiO_2$	1.46	0.26	0.37	0.91	0.05	0.3
Ir_{SA}-$CoNiO_2$	1.61	0.27	0.36	0.9	0.18	0.58

Table S6 ECSA data of CoNi alloy, V_O-$CoNiO_2$, Ir_{SA}-V_O-$CoNiO_2$ and Ir_{SA}-$CoNiO_2$ in OER tests.

Catalysts	C_{dl} (mF cm^{-2})	ECSA (cm^2)
CoNi	16.4	274
V_O-$CoNiO_2$	23.4	390
Ir_{SA}-V_O-$CoNiO_2$	29.1	485
Ir_{SA}-$CoNiO_2$	24.7	411

Table S7 Comparison of the mass activity performance with previously reported noble-metal base catalysts.

Catalysts	overpotential (mV)	mass activity(A mg^{-1})	Ref
Ir_{SA}-V_O-$CoNiO_2$	300	5 A mg_{Ir}^{-1}	This work
$Ir/Ni(OH)_2$	264	1 A mg_{Ir}^{-1}	Ref[10]
$Ir_1Co_{13.3}O_{20.1}$	255	1.412 A mg_{Ir}^{-1}	Ref[11]
Ir_1–$Ni(OH)_2$	300	1.867 A mg_{Ir}^{-1}	Ref[12]
$Ir_{0.06}Co_{2.94}O_4$	300	2.511 A mg_{Ir}^{-1}	Ref[13]
Ir-MoO_3	200	0.1789 A mg_{Ir}^{-1}	Ref[14]
Ir_1/V_O-CoOOH	300	605.4 A mg_{CoOOH}^{-1}	Ref[4]
^{s}Au/NiFe LDH	280	64.9 A $g_{NiFe\ LDH}^{-1}$	Ref[9]

Table S8 Comparison of the oxygen evolution performance performance compared to previously reported catalysts.

Catalysts	overpotential (mV) @ j = 10 mA cm^{-2}	Electrolyte	Ref.
Ir_{SA}-V_O-$CoNiO_2$	183	1.0 M KOH	This work
$Ir_{0.1}/Ni_9Fe$	183	1.0 M KOH	Ref[15]
Ir@IrNiO	195	1.0 M KOH	Ref[16]
np-Ir/NiFeO	197	1.0 M KOH	Ref[17]
$NiFeIr_{0.03}$/Ni NW@NSs	200	1.0 M KOH	Ref[7]
Ir_1/V_O-CoOOH	200	1.0 M KOH	Ref[4]
NiCoFe@NiCoFeO	201	1.0 M KOH	Ref[18]
$Ir_1/CoOOH_{sur}$	210	1.0 M KOH	Ref[6]
$Ir_{18\%}$-NiO	215	1.0 M KOH	Ref[3]
$Ir/Ni(OH)_2$	224	1.0 M KOH	Ref[10]
$Ir_1/Co_{0.8}Fe_{0.2}Se_2$	230	1.0 M KOH	Ref[19]
CoIr-0.2	235	1.0 M KOH	Ref[20]
Ir_1-$Ni(OH)_2$	260	1.0 M KOH	Ref[12]
Ir_1@Co/NC	260	1.0 M KOH	Ref[21]
Ir_1/T_O-CoOOH	270	1.0 M KOH	Ref[4]
Ir@Co nanosheets	273	1.0 M KOH	Ref[22]
$Ir@Co_3O_4$	280	0.1 M KOH	Ref[23]
CFFeSO	192	1.0 M KOH	Ref[24]
Ru SAs/AC-FeCoNi	205	1.0 M KOH	Ref[25]
EA-FCCN	211	1.0 M KOH	Ref[26]
LiNiFe borophosphate	215	1.0 M KOH	Ref[27]
ENWs-FeNi-C_2O_4	215	1.0 M KOH	Ref[28]
ML-NiFe LDH	217	1.0 M KOH	Ref[29]
FeNi-O/H	230	1.0 M KOH	Ref[30]
$Co_5Fe_3Cr_2OOH$	232	1.0 M KOH	Ref[31]

Fe-ZnMOFS	240	1.0 M KOH	Ref[32]
MoNiFe-27%OOH	242	1.0 M KOH	Ref[33]
RuCo/ELCO	247	1.0 M KOH	Ref[8]
Cu-CoP	252	1.0 M KOH	Ref[34]
FeCoNiPB	253	1.0 M KOH	Ref[35]
NiO/Co_3O_4	262	1.0 M KOH	Ref[36]
$FeNi-Mo_2C/C$	288	1.0 M KOH	Ref[37]
Aza-CMP-Co	289	1.0 M KOH	Ref[38]
$Vo-MnCo_2O_4$	290	1.0 M KOH	Ref[39]
2D/2D BNHNSs	297	1.0 M KOH	Ref[40]
Pt@N/C-10	298	1.0 M KOH	Ref[41]
$La(CrMnFeCo_2Ni)O_3$	325	1.0 M KOH	Ref[42]
CoPIm	334	1.0 M KOH	Ref[43]
$FeOOH-LaNiO_3$	350	1.0 M KOH	Ref[44]

References

1 D. K. Mann, J. Xu, N. E. Mordvinova, V. Yannello, Y. Ziouani, N. Gonzalez-Ballesteros, J. P. S. Sousa, O. I. Lebedev, Y. V. Kolen'ko and M. Shatruk, *Chem. Sci.*, 2019, **10**, 2796-2804.

2 Y. Chen, H. Li, J. Wang, Y. Du, S. Xi, Y. Sun, M. Sherburne, J. W. Ager, 3rd, A. C. Fisher and Z. J. Xu, *Nat. Commun.*, 2019, **10**, 572.

3 Q. Wang, X. Huang, Z. L. Zhao, M. Wang, B. Xiang, J. Li, Z. Feng, H. Xu and M. Gu, *J. Am. Chem. Soc.*, 2020, **142**, 7425-7433.

4 Z. Zhang, C. Feng, D. Wang, S. Zhou, R. Wang, S. Hu, H. Li, M. Zuo, Y. Kong, J. Bao and J. Zeng, *Nat. Commun.*, 2022, **13**, 2473.

5 H. You, D. Wu, D. Si, M. Cao, F. Sun, H. Zhang, H. Wang, T. F. Liu and R. Cao, *J. Am. Chem. Soc.*, 2022, **144**, 9254-9263.

6 C. Feng, Z. Zhang, D. Wang, Y. Kong, J. Wei, R. Wang, P. Ma, H. Li, Z. Geng, M. Zuo, J. Bao, S. Zhou and J. Zeng, *J. Am. Chem. Soc.*, 2022, **144**, 9271.

7 X. Luo, X. Wei, H. Zhong, H. Wang, Y. Wu, Q. Wang, W. Gu, M. Gu, S. P. Beckman and C. Zhu, *ACS Appl. Mater. Interfaces*, 2020, **12**, 3539-3546.

8 X. Zheng, J. Yang, Z. Xu, Q. Wang, J. Wu, E. Zhang, S. Dou, W. Sun, D. Wang and Y. Li, *Angew. Chem. Int. Ed. Engl.*, 2022, 202205946.

9 J. Zhang, J. Liu, L. Xi, Y. Yu, N. Chen, S. Sun, W. Wang, K. M. Lange and B. Zhang, *J. Am. Chem. Soc.*, 2018, **140**, 3876-3879.

10 G. Zhao, P. Li, N. Cheng, S. X. Dou and W. Sun, *Adv. Mater.*, 2020, **32**, 2000872.

11 C. Cai, M. Wang, S. Han, Q. Wang, Q. Zhang, Y. Zhu, X. Yang, D. Wu, X. Zu, G. E. Sterbinsky, Z. Feng and M. Gu, *ACS Catal.*, 2020, **11**, 123-130.

12 Q. He, S. Qiao, Q. Zhou, Y. Zhou, H. Shou, P. Zhang, W. Xu, D. Liu, S. Chen, X. Wu and L. Song, *Nano Lett.*, 2022, **22**, 3832-3839.

13 J. Shan, C. Ye, S. Chen, T. Sun, Y. Jiao, L. Liu, C. Zhu, L. Song, Y. Han, M. Jaroniec, Y. Zhu, Y. Zheng and S. Z. Qiao, *J. Am. Chem. Soc.*, 2021, **143**, 5201-5211.

14 X. Liu, S. Xi, H. Kim, A. Kumar, J. Lee, J. Wang, N. Q. Tran, T. Yang, X. Shao, M. Liang, M. G. Kim and H. Lee, *Nat. Commun.*, 2021, **12**, 5676.

15 X. Zheng, J. Tang, A. Gallo, J. A. Garrido Torres, X. Yu, C. J. Athanitis, E. M. Been, P. Ercius, H. Mao, S. C. Fakra, C. Song, R. C. Davis, J. A. Reimer, J. Vinson, M. Bajdich and Y. Cui, *Proc. Natl. Acad. Sci. U.S.A.*, 2021, **118**, 2101817118.

16 M. Liu, Y. Ji, Y. Li, P. An, J. Zhang, J. Yan and S. F. Liu, *Small*, 2021, **17**, 2102448.

17 K. Jiang, M. Luo, M. Peng, Y. Yu, Y. R. Lu, T. S. Chan, P. Liu, F. M. F. de Groot and Y. Tan, *Nat. Commun.*, 2020, **11**, 2701.

18 Y. Liu, Y. Ying, L. Fei, Y. Liu, Q. Hu, G. Zhang, S. Y. Pang, W. Lu, C. L. Mak, X. Luo, L. Zhou, M. Wei and H. Huang, *J. Am. Chem. Soc.*, 2019, **141**, 8136-8145.

19 Z. Zhang, C. Feng, C. Liu, M. Zuo, L. Qin, X. Yan, Y. Xing, H. Li, R. Si, S. Zhou and J. Zeng, *Nat. Commun.*, 2020, **11**, 1215.

20 Y. Zhang, C. Wu, H. Jiang, Y. Lin, H. Liu, Q. He, S. Chen, T. Duan and L. Song, *Adv. Mater.*, 2018, **30**, 1707522.

21 W. H. Lai, L. F. Zhang, W. B. Hua, S. Indris, Z. C. Yan, Z. Hu, B. Zhang, Y. Liu, L. Wang, M. Liu, R. Liu, Y. X. Wang, J. Z. Wang, Z. Hu, H. K. Liu, S. L. Chou and S. X. Dou, *Angew. Chem. Int. Ed. Engl.*, 2019, **58**, 11868-11873.

22 D. D. Babu, Y. Huang, G. Anandhababu, X. Wang, R. Si, M. Wu, Q. Li, Y. Wang and J. Yao, *J. Mater. Chem.*

A, 2019, **7**, 8376-8383.

23 Y. Dai, J. Yu, J. Wang, Z. Shao, D. Guan, Y. C. Huang and M. Ni, *Adv. Funct. Mater.*, 2022, **32**, 2111989.

24 W. H. Lee, M. H. Han, Y. J. Ko, B. K. Min, K. H. Chae and H. S. Oh, *Nat. Commun.*, 2022, **13**, 605.

25 Y. Hu, G. Luo, L. Wang, X. Liu, Y. Qu, Y. Zhou, F. Zhou, Z. Li, Y. Li, T. Yao, C. Xiong, B. Yang, Z. Yu and Y. Wu, *Adv. Energy Mater.*, 2020, **11**, 2002816.

26 N. Zhang, X. Feng, D. Rao, X. Deng, L. Cai, B. Qiu, R. Long, Y. Xiong, Y. Lu and Y. Chai, *Nat. Commun.*, 2020, **11**, 4066.

27 J. Kwon, H. Han, S. Jo, S. Choi, K. Y. Chung, G. Ali, K. Park, U. Paik and T. Song, *Adv. Energy Mater.*, 2021, **11**, 2100624.

28 X. Qiao, H. Kang, Y. Li, K. Cui, X. Jia, X. Wu and W. Qin, *Small*, 2022, **18**, 2106378.

29 Z. Zheng, D. Wu, G. Chen, N. Zhang, H. Wan, X. Liu and R. Ma, *Carbon Energy*, 2022.

30 X. Gu, Z. Liu, M. Li, J. Tian and L. Feng, *Appl. Catal. B*, 2021, **297**, 120462.

31 J. Chen, H. Li, S. Chen, J. Fei, C. Liu, Z. Yu, K. Shin, Z. Liu, L. Song, G. Henkelman, L. Wei and Y. Chen, *Adv. Energy Mater.*, 2021, **11**, 2003412.

32 Y. Wang, L. Zhao, J. Ma and J. Zhang, *Energy Environ. Sci.*, 2022.

33 Z. He, J. Zhang, Z. Gong, H. Lei, D. Zhou, N. Zhang, W. Mai, S. Zhao and Y. Chen, *Nat. Commun.*, 2022, **13**, 2191.

34 D. Thiyagarajan, M. Gao, L. Sun, X. Dong, D. Zheng, M. Abdul Wahab, G. Will and J. Lin, *Chem. Eng. J.*, 2022, **432**, 134303.

35 Q. Wang, J. Li, Y. Li, G. Shao, Z. Jia and B. Shen, *Nano Research*, 2022.

36 J. Zhang, J. Qian, J. Ran, P. Xi, L. Yang and D. Gao, *ACS Catal.*, 2020, **10**, 12376-12384.

37 M. Wang, Y. Wang, S. S. Mao and S. Shen, *Nano Energy*, 2021, **88**, 106216.

38 H. Yang, F. Li, S. Zhan, Y. Liu, W. Li, Q. Meng, A. Kravchenko, T. Liu, Y. Yang, Y. Fang, L. Wang, J. Guan, I. Furó, M. S. G. Ahlquist and L. Sun, *Nat. Catal.*, 2022, **5**, 414-429.

39 K. Zeng, W. Li, Y. Zhou, Z. Sun, C. Lu, J. Yan, J.-H. Choi and R. Yang, *Chem. Eng. J.*, 2021, **421**, 127831.

40 J. Mei, J. Shang, T. He, D. Qi, L. Kou, T. Liao, A. Du and Z. Sun, *Adv. Energy Mater.*, 2022, 2201141.

41 H. G. R. Monestel, I. S. Amiinu, A. A. González, Z. Pu, B. Mousavi and S. Mu, *Chinese J. Catal.*, 2020, **41**, 839-846.

42 T. X. Nguyen, Y. C. Liao, C. C. Lin, Y. H. Su and J. M. Ting, *Adv. Funct. Mater.*, 2021, **31**, 2101632.

43 Piyali Bhanja, Yena Kim, Kenya Kani and B. Paul, *Chem. Eng. J.*, 2020, **396**, 125245.

44 J. W. Zhao, C. F. Li, Z. X. Shi, J. L. Guan and G. R. Li, *Research*, 2020, **2020**, 6961578.